Journal of Materials Research and Technology 41 (2026) 6202–6210

Contents lists available at ScienceDirect

Journal of Materials Research and Technology

journal homepage: www.elsevier.com/locate/jmrt

Microstructure refinement and bicontinuity formation by distributed internal melting at the Ni_3Sn_4 peritectic

Zhongyang Li [a],*, Lukas Lührs [a], Jörg Weissmüller [a,b]

[a] Institute of Materials Physics and Technology, Hamburg University of Technology, Hamburg, Germany
[b] Institute of Hydrogen Technology, Helmholtz-Zentrum Hereon, Geesthacht, Germany

ARTICLE INFO

Keywords:
Liquid-metal dealloying
Peritectic melting
Liquid film migration
NiSn alloy
Constitutional supercooling

ABSTRACT

Guided by a current interest in processing schemes, such as liquid-metal dealloying, providing fine-scale bicontinuous metal microstructures, we investigate the microstructure evolution during the peritectic melting of Ni_3Sn_4. The product microstructure is an interconnected array of spherical clusters of crystallographically aligned Ni_3Sn_2 ligaments, interpenetrated by a contiguous liquid phase. When quenched to room temperature, the prevalent microstructure consists of two interpenetrating solid phases. Leaching the solidified Sn melt produces monolithic porous bodies of Ni_3Sn_2. The characteristic structure size can reach down to 2 μm, a microstructure refinement by almost 2 orders of magnitude as compared to the 150 μm grain size of the master alloy. Remarkably, a more severe refinement is achieved at higher annealing temperatures. Our experiments identify liquid-film migration as the controlling process, here concurrent with constitutional supercooling and cellular solidification. We argue that peritectic melting exemplifies a more general family of processes of distributed internal melting (DIM). These processes exploit the abundant nucleation of regions of melt, finely distributed throughout a parent microstructure, when the alloy is heated into a two-phase solid–liquid regime of its phase diagram. DIM provides a novel and versatile pathway to fine-scale bicontinuous microstructures.

1. Introduction

As a well-developed and topical dealloying technique, liquid-metal dealloying (LMD) generates micro- or nanoscale porous materials such as Ti [1,2], Nb [3,4], Ta [5], stainless steel [6] or high entropy alloys [7,8]. During LMD, the dissolving constituent, driven by the negative enthalpy of mixing, diffuses from the parent alloy into the melt. The conserved constituent reorganizes by surface diffusion along the dealloying front. In this way, the originally uniform parent alloy is converted into a bicontinuous structure, defined by two interpenetrating and contiguous phases [9]. A porous metal network can be obtained by selectively etching one phase.

Recent studies on the intermetallic compound TiAg [10,11] have revealed that a bicontinuous structure, similar to the product of LMD, can be obtained by peritectic melting (reverse peritectic reaction). When heated above the peritectic temperature, TiAg decomposes into Ti solid solution and Ag melt, forming a bicontinuous composite with a dealloying-like microstructure. This approach is similar to LMD, as both processes operate in a semisolid state and result in similar microstructures. However, unlike LMD, peritectic melting acts locally, with no need for mass exchange with the environment. This mitigates the transport-imposed restrictions on sample size inherent in LMD.

The attractive aspects of bicontinuous microstructure generation by peritectic melting raises the question whether the process, rather than being restricted to TiAg, may be transferred to other alloy systems. Furthermore, one may ask in how far the transformation mechanisms are generic for peritectic melting and in how far they agree with those acting during LMD. The present study demonstrates that TiAg is indeed not the sole eligible compound. It also reveals that the transformation process and the mechanisms promoting microstructure refinement may differ between peritectic reactions in different alloy systems and between peritectic melting and LMD.

Initially, the microstructure formation during peritectic melting of TiAg was attributed to a dealloying-like process [10], but further study has established that the bicontinuous structure is formed by the migration of liquid films [11]. Liquid film migration (LFM) has been extensively studied in the context of partial melting; alloy systems include Mo-Ni [12,13], Al-Cu [14,15], Co-Cu [16], Cu-In [17,18]. Several ceramic systems have also been investigated [19,20]. When the alloy is heated into the solid–liquid two phase region, the grain boundary of a parent grain retreats as atoms dissolve into the liquid layer, and the newly formed grain solidifies from the melt and with a close-to-equilibrium composition [13]. The same mechanism has also been

* Corresponding author.
E-mail address: zhongyang.li@tuhh.de (Z. Li).

https://doi.org/10.1016/j.jmrt.2026.02.189
Received 5 January 2026; Accepted 22 February 2026
Available online 23 February 2026

observed in other processes, such as sintering [21,22], welding [23,24], and during solidification [25–27]. For peritectic melting, LFM has been investigated through phase field simulations [28,29], and evidence of LFM during peritectic melting has been found in certain systems [11, 30].

The action of LFM in forming bicontinuous microstructures has been studied in both partial melting [18] and peritectic melting [11]. There are notable similarities between these two processes, as both involve the decomposition of a solid parent phase into a new solid product phase and the melt. During partial melting of a Cu-In alloy [18], the newly formed Cu solid solution is initially deposited onto the parent phase, as both share the same crystal structure. Similarly, during peritectic melting of TiAg [11], the newly formed Ti phase nucleates at the interface of the TiAg parent with the melt, with a preferred crystal orientation. Partial and peritectic melting share the same mechanism (namely liquid film migration) for parent-phase decomposition and for nucleation (heterogeneous nucleation) of the new solid phase, and both processes produce similar bicontinuous microstructures.

Our search for alternative peritectics highlighted Ni_3Sn_4 as a particularly interesting case. Spherical clusters of fine Ni_3Sn_2 ligaments were observed, which is distinct from all peritectic or partial melted structures reported in previous studies. The unique microstructure and significant structure refinement cannot be explained solely by LFM. In this work, we discuss the growth mechanism of the new phase and factors affecting the final microstructure, which had not previously been linked to peritectic melting. As a key process, we identify the abundant appearance of regions of the melt, distributed uniformly throughout the alloy microstructure. This facilitates the finely dispersed nucleation of the new solid phase and its growth by precipitation from the melt, a prerequisite for a uniform and small-scale microstructure. As our findings demonstrate, such distributed internal melting (DIM) processes, exemplified by peritectic melting or partial melting, provide an attractive alternative to LMD when it comes to producing micro-scale bicontinuous microstructures.

2. Experimental details

Ingots of the intermetallic compound Ni_3Sn_4 were made by arc-melting Ni (>99.98%) wire and Sn (>99.999%) granules in an Ar atmosphere. To obtain a homogeneous Ni_3Sn_4 phase, the ingots were sealed in quartz tubes under vacuum (approximately 30 Pascal) and homogenized at 700 °C for 7 days, followed by furnace cooling. The homogenized ingots were cut into cuboid samples, $1 \times 1 \times 2$ mm in size. Peritectic melting was performed in a tube furnace in air. The samples were placed into a preheated crucible and inserted into the furnace, heated at 820 °C or 1000 °C for various durations and then quenched by rapid immersion into room-temperature water. The temperature of the furnace chamber was monitored with a thermocouple, the insertion of the sample causes less than 10 degrees of fluctuation. Fast sample insertion and extraction are essential for defining the annealing time and for preserving the high-temperature microstructure during quenching. In the interest of rapid insertion and extraction, peritectic melting was performed in air rather than in vacuum or protective gas.

Microstructure observation and phase identification were carried out using scanning electron microscopy (SEM, Zeiss Supra VP55), equipped with an energy dispersive spectroscopy (EDS) unit. Images were taken in the central area of the samples for better representation of the microstructure and minimization of the oxidation effect. The samples were first embedded in epoxy, then ground using abrasive paper in the following grit sequence: 320, 600, 1200, 2500, 4000. Subsequently, these samples were polished in colloidal silica suspension, then cleaned with ethanol to reveal the cross-sectional surface. Ligament sizes were determined, for any particular sample quality, by averaging the thickness values, determined by the use of ImageJ [31], of at least 150 ligaments. The same software was used for measuring the area fraction – representative of the phase fraction – of different phases in binarized SEM images.

Table 1
EDS results of the as-quenched sample cross section in Fig. 3(b).

Position	Ni (at.%)	Sn (at.%)	Phase
1	54.7	45.3	Ni_3Sn_2
2	43.1	56.9	Ni_3Sn_4
3	2.4	97.6	Sn solid solution

For electron backscatter diffraction (EBSD), the samples were further polished using ion milling to reduce surface stress. The EBSD experiments were conducted on the Zeiss Supra VP55, and further analyzed with AzTec HKL (Oxford instruments) and Channel 5 (HKL Technology, co.) softwares. Crystal structure data were adopted from crystallography open database [32].

In etched samples, the Sn solid solution was selectively removed via electrochemical etching in 0.5 M H_2SO_4 at −0.6 V against a homemade Ag/AgCl reference electrode, without harming the Ni_3Sn_2 and Ni_3Sn_4 phases. Then the samples were cleaned with ethanol and fractured with a scalpel to create a fracture surface that formed the basis for SEM observation.

3. Results

3.1. Microstructure after peritectic melting

The relevant part of the phase diagram of Ni-Sn system is shown in Fig. 1(a). It includes the peritectic reaction, Ni_3Sn_2 HT ($P6_3/mmc$ [34]) + Liquid → Ni_3Sn_4 (C12/m1 [35]) at 798 °C. For simplicity, all types of Ni_3Sn_2 phases will be collectively referred to as Ni_3Sn_2, as distinguishing these phases is not the primary focus of this study.

Fig. 1(b) and (c) show the microstructure of the homogenized parent alloy. Besides pores (black contrast), which are casting defects formed during solidification, the two solid phases observed in Fig. 1(c) are Ni_3Sn_4 (darker gray) as the dominant phase and a small amount of Sn (lighter gray) at grain boundaries and triple points. The homogenized structure agrees with the phase diagram, with the residual Sn suggesting a small deviation of our alloy from the true peritectic composition.

EBSD (Fig. 2) shows that the homogenized sample is polycrystalline with a grain size of approximately 150 μm. The inverse pole figure of Ni_3Sn_4, Fig. 2(b), gives no evidence of texture.

The homogenized samples were annealed at 820 °C, around 20 K above the peritectic temperature, for various durations, then quenched in room temperature water. According to the phase diagram, the quenched sample should contain Ni_3Sn_2, which is the solid phase at high temperature, as well as Sn solid solution, which is the solidified melt. Representative cross-sectional electron micrographs in Fig. 3(a) and (b) reveal three distinct phases. The bright regions correspond to Sn solid solution, as Sn atoms, having a higher atomic number, exhibit brighter contrast in backscattered electron (BSE) images. The EDS results in Table 1 suggest that the dark phase is Ni_3Sn_2. The morphology of that phase is similar to that of ligaments in dealloyed porous metals. A gray phase is located at the surface of Ni_3Sn_2 and embedded in the Sn phase. EDS identifies that phase as Ni_3Sn_4; the phase diagram suggests that it precipitates from the melt during cooling. Contrast within the Ni_3Sn_2 regions may be attributed to differences in crystal orientation. We emphasize that the just-described microstructural morphology extends consistently throughout the investigated cross-sections of several samples prepared in this manner.

For a clearer view of the ligament structure, the Sn solid solution was selectively etched from a sample that had undergone peritectic melting. That process achieved the complete removal of the Sn solid solution phase. This demonstrates that the Sn phase is contiguous. Furthermore, we found that the sample remained physically connected

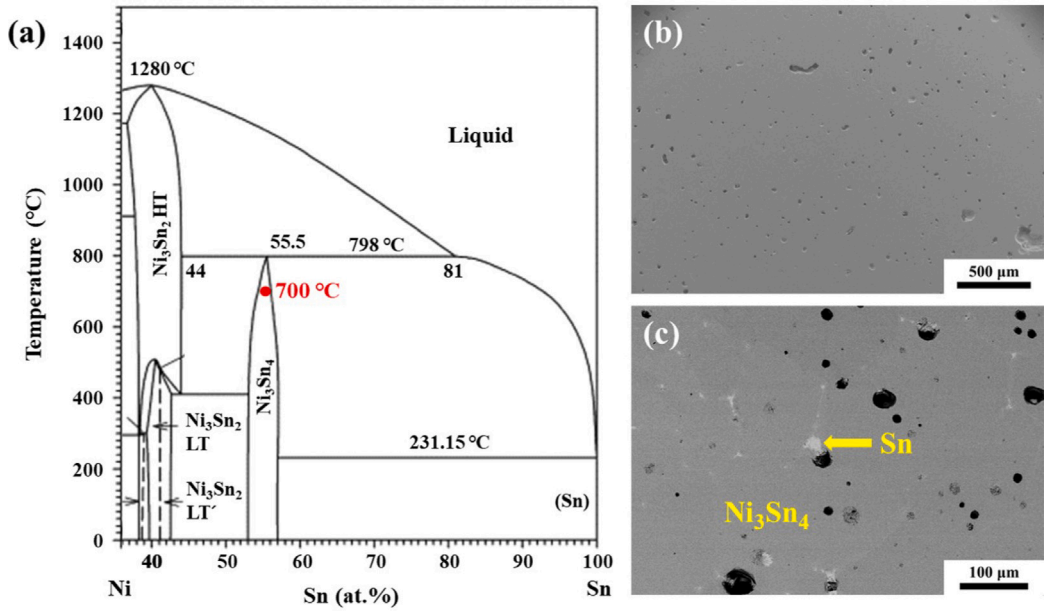

Fig. 1. Microstructure of the homogenized sample. (a) The relevant part of Ni-Sn phase diagram, redrawn after [33]. Red spot shows master alloy composition and homogenization temperature at 700 °C. (b) Secondary electron image of the homogenized sample, large pores formed during solidification can be observed. (c) Enlarged backscattered electron image of the as-homogenized sample. Gray phase is Ni_3Sn_4, bright phase which distributes at grain boundaries and triple points is Sn, and dark areas are identified as pores.

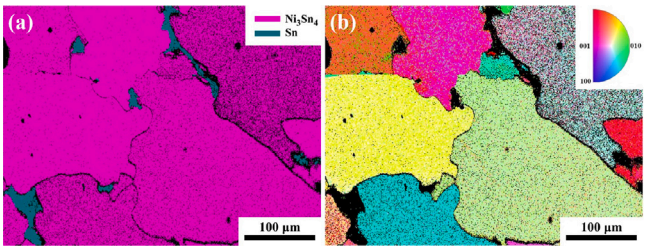

Fig. 2. Electron backscatter diffraction results of a homogenized sample. (a) Phase distribution. (b) Inverse pole figure of the homogenized sample, only data of Ni_3Sn_4 phase is shown.

Table 2
Composition of center and surface areas of the ligaments in the etched, porous sample of Fig. 3(d).

Position	Ni (at.%)	Sn (at.%)	Phase
1	55.4	44.6	Ni_3Sn_2
2	53.5	46.5	Ni_3Sn_2
3	44.0	56.0	Ni_3Sn_4
4	45.2	54.8	Ni_3Sn_4

after the Sn removal. This implies that the remaining, complementary phase is also contiguous. Clearly, a bicontinuous structure was formed after peritectic melting and quenching.

The microstructure at a cross-section of the etched, porous sample was revealed by cleaving the sample with a scalpel. The micrographs in Fig. 3(c, d) here show Ni_3Sn_2 ligaments covered by Ni_3Sn_4. The phase identification is supported by EDS results (Table 2) of the central and surface area of the ligaments.

The EBSD phase identification of an as-quenched sample, Fig. 4(a), shows Ni_3Sn_2 coexisting with the Sn solid solution phase. Ni_3Sn_4 regions are here too small for identification. The inverse pole figure of only the Ni_3Sn_2 phase, Fig. 4(b), shows large clusters of ligaments with the same crystallographic orientation. This indicates that the ligaments, seemingly isolated in 2D images, are in fact interconnected parts of the same crystal grain. The grain size suggested by this observation is 50 to 100 µm, which is similar to the grain size of the initial, homogenized alloy. Note, however, that the characteristic size of the ligaments is substantially smaller (less than 10 µm). This implies a drastic microstructural refinement after peritectic melting and resolidification.

3.2. Effect of temperature on the microstructure

Besides the 820 °C runs, peritectic melting was also performed at 1000 °C and the impact of the annealing temperature on the final microstructure is studied. At the higher annealing temperature, the decomposition of Ni_3Sn_4 is completed within a shorter time. In order to minimize the impact of post-decomposition coarsening, and to explore the smallest structure size that can be obtained by the reverse peritectic reaction, we here compare microstructures right after complete decomposition. To identify that point, peritectic melting tests with various annealing durations were performed at each temperature. The cross sections of these samples were then examined to search for residual undecomposed Ni_3Sn_4 phase. Our observation suggests that the decomposition was just completed after 20 s of heating at 820 °C, while only 3 s were required at 1000 °C. The microstructure evolution observed in samples annealed at 820 °C and 1000 °C is shown in Fig S1 and S2 of the Supporting Information (SI).

We observed only a thin oxide layer at the sample surface after peritectic melting (see Fig S3). The element mapping of different sample areas (see Fig S4 and S5) suggests a homogeneous distribution of oxygen content after peritectic melting, which is likely the result of surface oxidation during preparation of metallographic samples. The oxidation effect is not prominent, given the short heating durations (3 s up to 40 s).

The microstructures right after complete decomposition at the two temperatures are compared side-by-side in Figs. 5(a) and (b). Their morphologies appear quite similar. For the sample annealed at 1000 °C, the area fraction of the solidified melt phase (measured from SEM images) is 0.35 ± 0.01, slightly higher than the 0.30 ± 0.02 for the 820 °C sample. This is not unexpected, in view the phase fraction trend inferred from the alloy phase diagram. However, the impact of the

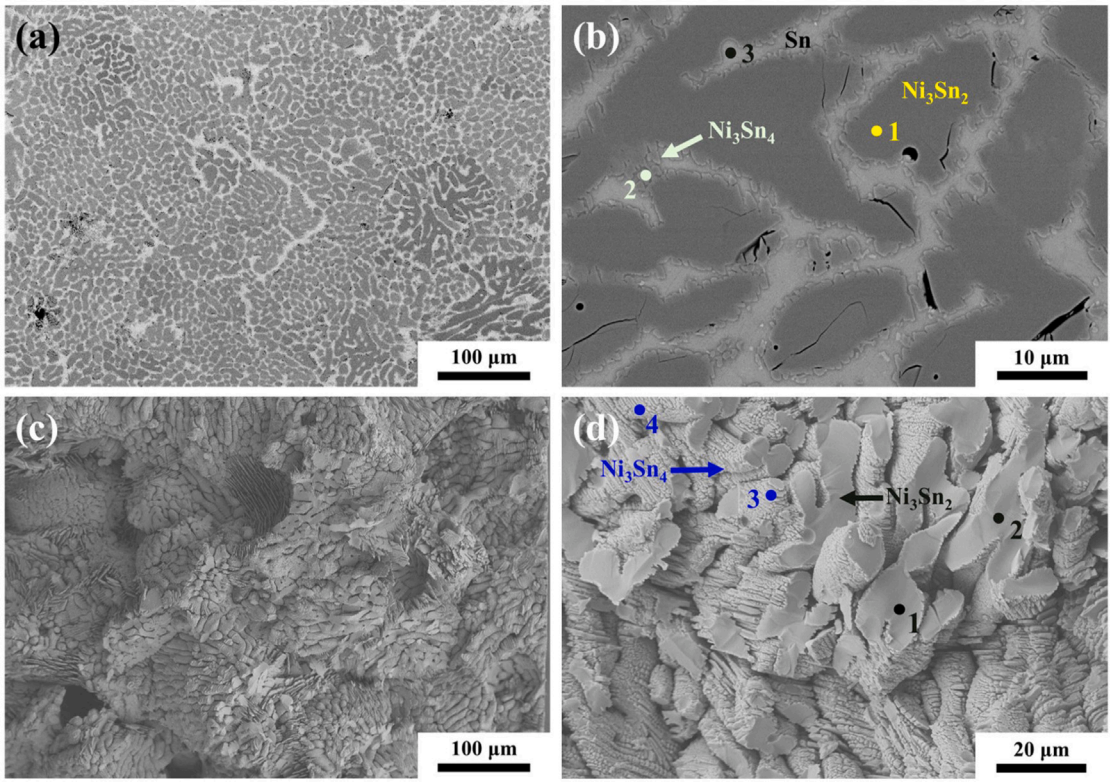

Fig. 3. Scanning electron micrographs of microstructure after heating at 820 °C for 40 s. (a, b) As-quenched sample. Backscattered electron images of ground and polished cross-section. Bright phase: Sn solid solution; dark phase: Ni_3Sn_2 with ligament morphology; gray phase covering Ni_3Sn_2 ligaments: Ni_3Sn_4. Indexed points in (b) designate location of EDX in Table 1 (c, d) Porous sample after removal of Sn by electrochemical corrosion. Secondary electron images of cleavage surface. Indexed points in (d) designate location of EDX in Table 2.

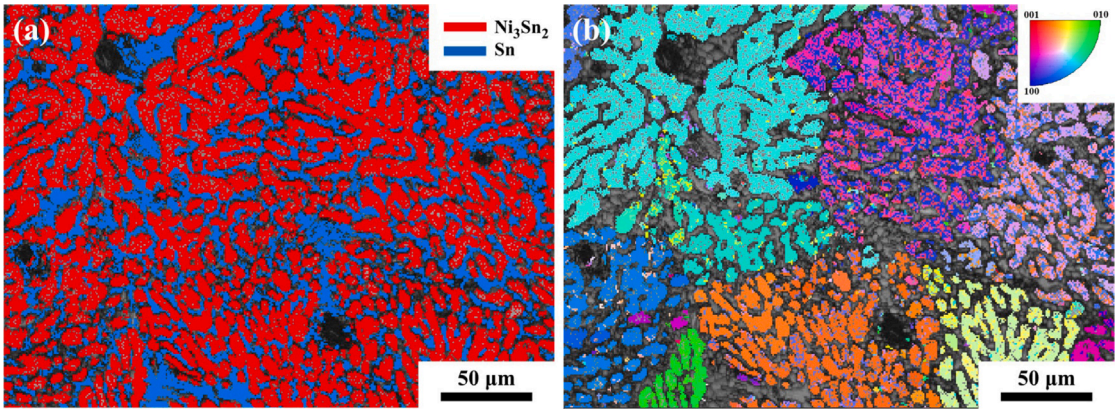

Fig. 4. Electron backscatter diffraction characterization of a sample after heating at 820 °C for 40 s. (a) Phase distribution of Ni_3Sn_2 and Sn solid solution. (b) Inverse pole figure of only Ni_3Sn_2 phase. Different ligaments with the same orientation suggest that they are actually interconnected. Ni_3Sn_4 was not detected due to the small size.

temperature change on the microstructural length scale is remarkable. Increasing the annealing temperature reduces the ligament size and the spacing between ligaments. In fact, at 2.1 ± 0.5 μm, the ligament size of the sample annealed at 1000 °C is less than half that of the 820 °C sample, 4.6 ± 1.1 μm. The evolution from an initial microstructural length scale of approximately 150 μm (the master alloy grain size) to a final ~2 μm (the ligament size) represents a 75 fold microstructural refinement, which is remarkable for a high-temperature process.

3.3. Microstructure of partially decomposed samples

A partially decomposed sample was obtained by annealing at 820 °C for 15 s, followed by quenching in room temperature water. The cross-sectional microstructure is shown in Fig. 6. Undecomposed Ni_3Sn_4 grains can be observed alongside the decomposed microstructure. Grain boundaries between those grains appear completely wetted by the Sn phase, which is the melt at the temperature of the peritectic decomposition. The micrographs also show convex regions – apparently globular

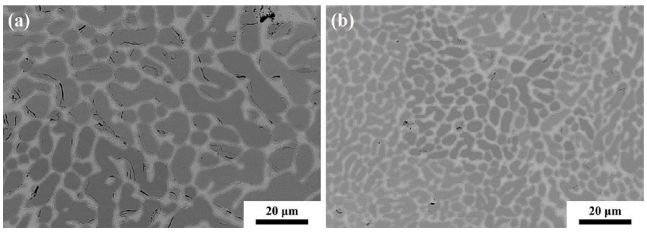

Fig. 5. Impact of environmental temperature on characteristic microstructural length scale in samples quenched right after completion of reverse peritectic reaction. Backscattered electron images of the sample cross sections after (a) heating at 820 °C for 20 s, and (b) heating at 1000 °C for 3 s. Note smaller size at higher temperature.

in three dimensions – with the ligamentary Ni_3Sn_2/Sn morphology. These regions are the product of the reverse peritectic reaction (see Fig. 4). Fig. 6 shows that their interface with the as-yet undecomposed Ni_3Sn_4 grains is also completely wetted by Sn. This implies that the phase transformation is mediated by the consumption, at the advancing side of the liquid Sn film, of Ni_3Sn_4 and the precipitation, at the receding side, of Ni_3Sn_2, which is accompanied by partitioning of the components between the product solid and residual melt. We rate this as evidence of LFM.

The image area of Fig. 6(a) exhibits a gradient, with a higher degree of decomposition in the upper part of the image. That part was closer to the outer sample surface, suggesting faster heating and a somewhat longer exposure to the annealing temperature.

Fig. 6(b) is the enlarged image of the area outlined by the yellow rectangle in Fig. 6(a). The thin Sn layer which separates the undecomposed Ni_3Sn_4 grain from the newly formed Ni_3Sn_2 cluster is highlighted. The Ni_3Sn_2 cluster occupies a convex envelope, while the Ni_3Sn_4 grain is bounded by a concave surface. One notes that ligaments in the central area of the Ni_3Sn_2 cluster are larger compared to those at the periphery. Those observations support the notion of a decomposed two-phase region that advances into the original intermetallic, with the liquid film mediating the lateral partitioning of the components between the new solid compound and the melt.

Fig. 7 shows the EBSD characterization of the partially decomposed Ni_3Sn_4 sample. By inspection of the phase map (panel (a)) and the inverse pole figure (panel (b)), one perceives clearly that multiple Ni_3Sn_2 clusters have formed at one and the same grain boundary. The inverse pole figure (Fig. 7(b)) shows that the individual clusters exhibit different crystallographic orientation.

4. Discussion

4.1. Liquid-film migration

The discussion of our observations starts out with contrasting liquid film migration to liquid-metal dealloying.

When investigating partially decomposed samples (see Fig. 6), we observe Ni_3Sn_2 clusters with a convex envelope that must be identified with their growth front. The clusters are embedded in partially decomposed Ni_3Sn_4 grains with a concave surface that must be the receding melting front. A Sn layer (the solidified melt) separates the parent phase from the solid product phase. Obviously, the peritectic reaction is mediated by transport across the liquid film and by component partitioning between Ni_3Sn_2 and residual melt through lateral diffusion in the film. This confirms that the decomposition of Ni_3Sn_4 proceeds by a liquid-film migration (LFM) mechanism.

LFM involves the dissolution of the parent phase on the advancing side of the migrating liquid film, the transport of the product-phase components across the film and, on the receding side, their redeposition by accretion of lattice sites on a growing crystal of the product phase. By contrast, the microstructure formation during aqueous dealloying may be understood in terms of a redistribution of the more noble component by interface diffusion along the corrosion surface [36]. In that scenario, as two qualitative differences to LFM, (i) the component forming the product phase is not dissolved and (ii) the crystal lattice is conserved [37,38].

Arguably the most obvious qualitative difference between dealloying and LFM concerns the transport direction of the conserved/product-phase component(s). In LFM, that direction is normal to the interface. By contrast, dealloying relies on transporting the conserved component parallel to the interface, in order to form the ligaments of the new microstructure. Gradients, along the interface, in the mean curvature provide the underlying driving force. Parallel transport is also the mechanism behind the trend for passivation that prevents dealloying at too low driving force (below the "critical dealloying potential" [39, 40] in electrochemical dealloying) or too high atom fraction of the conserved component (beyond the parting limit [40,41]).

While aqueous dealloying typically relies on negligible solubility of the conserved component in the liquid, a significant role of dissolution and redeposition has been proposed for LMD. It is linked to the finite solubility of the nominally immiscible (conserved) component in the melt [42,43], specifically when enrichment of the miscible (sacrificial) element in the melt increases its solubility for the conserved element [42]. The presence of dissolution and redeposition has similarities to LFM. Yet, in contrast to LFM, typical LMD scenarios still have the conserved element transported parallel to the interface and deposited back onto the original crystal lattice. The consequences of the lateral transport for the corrosion mechanism and for the microstructure evolution in LMD are similar to those in aqueous dealloying [44]. An exception, with interesting parallels to LFM, is observed for local LMD processes near grain boundaries. Here, liquid films may be formed and both transport directions are observed, parallel and normal to the interface [43].

4.2. Growth of the product microstructure

The large clusters of crystallographically aligned Ni_3Sn_2 ligaments suggest comparatively scarce nucleation events, in the order of one nucleus per grain of the parent microstructure. The observation of the liquid film separating the parent and product intermetallic compounds in partially decomposed samples implies complete wetting of the nucleus by the melt.

A schematic illustrating the nucleation and growth process of Ni_3Sn_2 is shown on Fig. 8. Panel (a) illustrates an early-stage Ni_3Sn_2 precipitate, which is embedded in the liquid Sn of the wetting layer at the Ni_3Sn_4 grain boundaries. Panel (b) suggests melting of the Ni_3Sn_4 parent phase with no preferred direction, promoting an essentially spherical growth geometry of the precipitate. Panel (c) emphasizes the cellular growth of the Ni_3Sn_2 product phase, mediated by transport through the migrating liquid film at the interface with the parent phase.

A previous study of peritectic melting in TiAg [11] also identified liquid-film migration (LFM) as the underlying mechanism. In spite of that similarity, the resulting microstructures are quite distinct in TiAg and NiSn. In the former system, the Ti product phase exhibits convex rather than cellular grains, and these convex grains are always connected to a grain of the parent phase by a planar interface with a defined crystallographic orientation relationship. The low interfacial energy promotes heterogeneous nucleation of Ti at the TiAg/melt interface [11]. Our inspection of partially decomposed samples reveals no interface between Ni_3Sn_4 and Ni_3Sn_2. Homogeneous nucleation of the Ni_3Sn_2 phase could be one explanation of the absence of such an interface. Alternatively, our results do not exclude that Ni_3Sn_2 forms by heterogeneous nucleation and is later wetted by the Sn melt. In either scenario, the precipitates are eventually surrounded by the melt and their growth front propagates by LFM. This is illustrated by Fig. 8(c).

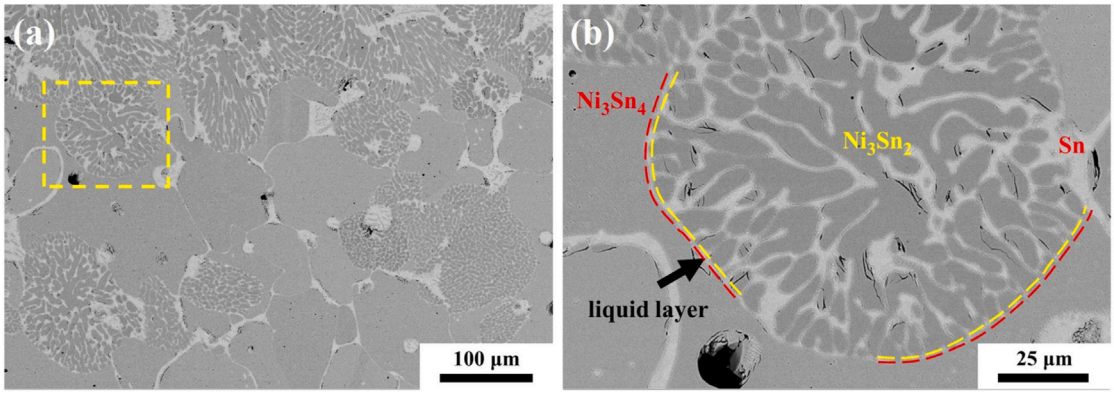

Fig. 6. Backscattered electron image of a partially decomposed sample. Sample heated at 820 °C for 15 s, then quenched in water. (a) Overview image, with a region of interest highlighted by dashed box. (b) Enlarged and marked display of the region of interest. Yellow dashed line, Ni_3Sn_2 growth front; red dashed line, Ni_3Sn_4 melting front. The dashed lines are broken for visibility of the solidified Sn melt, separating the fronts.

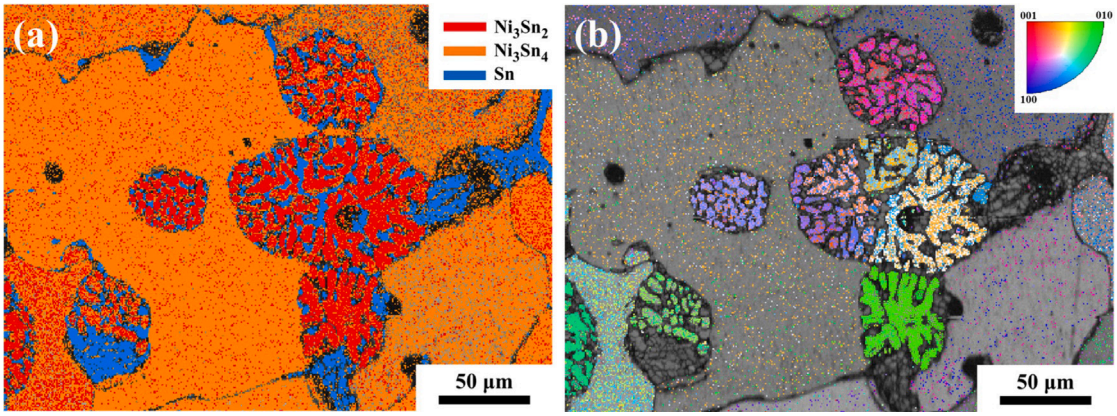

Fig. 7. Electron backscattered diffraction results of the central area of a partially decomposed sample (heated at 820 °C for 15 s before quenching). (a) Phase distribution of Ni_3Sn_2 clusters, undecomposed Ni_3Sn_4 and Sn. (b) Inverse pole figure of Ni_3Sn_2 clusters. Different orientation between these clusters can be detected.

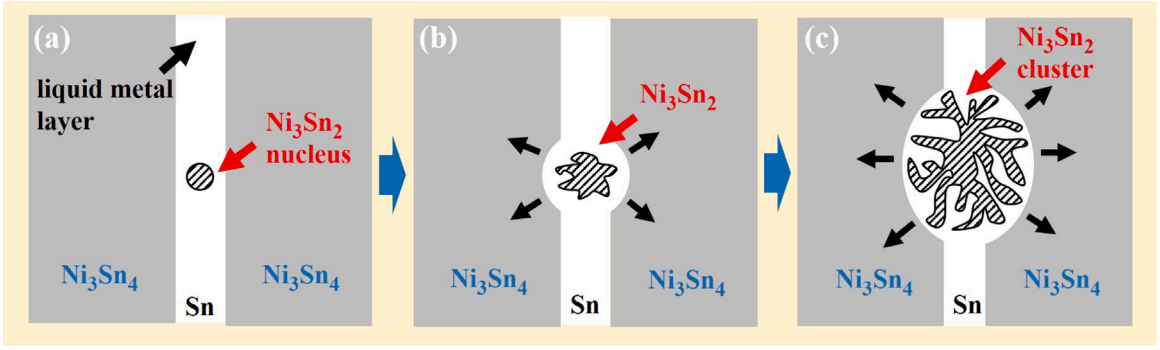

Fig. 8. Schematics of nucleation and growth process during peritectic melting of Ni_3Sn_4. The newly formed Ni_3Sn_2 phase nucleates inside the liquid metal layer at wetted grain boundaries, then grows in all direction at the expense of Ni_3Sn_4, eventually forms a cluster of Ni_3Sn_2 ligaments.

Interestingly, more than one orientation can be observed in the largest cluster in Fig. 7(b). This might happen when two nuclei form close to each other. The two nuclei initiate LFM at their nearest grain boundary, and then grow in opposite directions. The two clusters together form a large spherical cluster as in Fig. 7(b), in which two different orientations exist.

As a further characteristics of NiSn peritectic melting, we note that the ligament size is found larger in the center of the clusters. As nucleation and growth start out at the center, the Ni_3Sn_2 ligaments there form first and have more time for coarsening than the ligaments at the periphery of the clusters. The evidence of substantial coarsening suggests that the observed ligament spacing does not forcefully reflect the size selection during the initial solidification event.

4.3. Component partitioning

We now examine the origin of the cellular growth of the Ni_3Sn_2 clusters. For conciseness, the Ni_3Sn_2 product and the Ni_3Sn_4 parent phases are denoted as α and β, respectively, and the melt as L.

The conversion of β into α and L requires partitioning of the components at the reverse peritectic reaction front. For laterally extended reaction fronts, such scenarios – similar to eutectic solidification

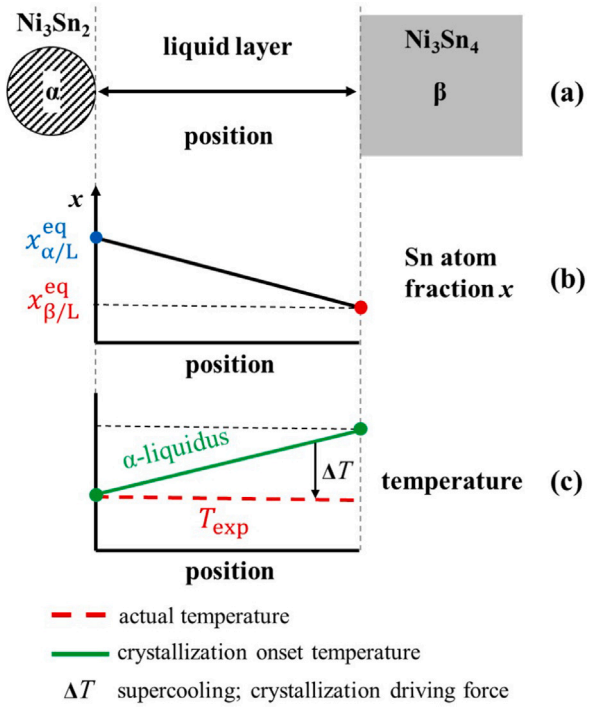

Fig. 9. Schematic of composition and temperature distribution in the melt. (a) Geometry of the growing and melting phases. The Ni_3Sn_2 nucleus and the Ni_3Sn_4 grain is separated by a liquid layer. (b) Composition (Sn) in the melt. (c) Temperature distribution in the liquid layer. Red dashed line shows actual temperature, while the green line represents the crystallization onset temperature of the melt. ΔT is the difference between these two temperatures, caused by constitutional supercooling.

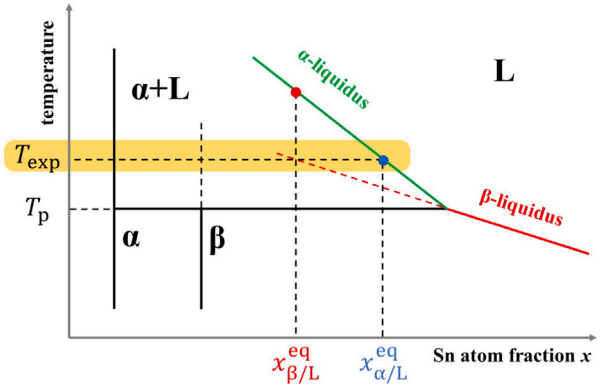

Fig. 10. Schematic of the Ni-Sn phase diagram at the peritectic reaction area. T_p is the peritectic temperature. The red dashed line is the extension of β liquidus line while the blue line is the α liquidus line. The constrained equilibrium at the annealing temperature T_{exp} at β and α surfaces are represented by the vertical dot lines. Decided by the constrained equilibrium, the melt composition at the β melting front and the α growth front are denoted as $x^{eq}_{\beta/L}$ and $x^{eq}_{\alpha/L}$.

– result in cellular structures. Our observations advertise the liquid film separating parent and product phase as the transport channel for component partitioning, which therefore relies on lateral diffusion in the melt.

A minimum thickness of the liquid film is required to afford sufficient transport cross-section for partitioning the components rapidly, keeping track with the progress of the melting and partial re-solidification of the reverse peritectic reaction. If the α solidification front were to progress faster than the melting front recedes, the liquid film would become thinner and surplus Sn could no longer be efficiently transported laterally to the melt channels. The liquid ahead of the solidification front would then enrich in Sn and eventually cross the α liquidus, stopping the solidification. That mechanism stabilizes the film thickness. These considerations emphasize that there must be an intricate interrelation between driving force from superheating, reaction front velocity, film thickness and cell spacing.

Our considerations are naturally compatible with the observation of smaller structures size at larger overheating. Higher environmental temperature leads to enhanced heat flux and, hence, more overheating and higher driving force for the reverse peritectic reaction. The process can then generate smaller structures, even though higher excess energy needs to be stored in the interfaces. We note that the driving force, promoting microstructure refinement, scales with the overheating, which is zero at the equilibrium peritectic temperature T_p. By contrast, the diffusivity – which promotes long-range lateral transport as well as coarsening and so opposes the microstructural refinement – starts with a finite value at T_p. Therefore, the relative increase of the driving force with T is initially always larger than the relative increase of the diffusivity, so the trend for refinement will initially prevail.

We now argue that constitutional supercooling might provide a mechanism for destabilizing an initially planar solidification front and initiating the formation of the cell structure. We consider a pre-existing α nucleus and a decomposing β grain, separated by the liquid film, as illustrated in Fig. 9(a). We assume local equilibrium at all solid/melt interfaces. With transport limitations preventing melting at equilibrium, right at the peritectic temperature T_p, we may take β as superheated above T_p. The local equilibrium at the interface between superheated β and L is then a constrained (no α) equilibrium, and the appropriate liquidus line is the extrapolated β liquidus. Fig. 10 schematically illustrates that line in an enlarged display of the peritectic region of the Ni–Sn phase diagram. At the experimental annealing temperature T_{exp}, the β-L equilibrium point is represented by the intersection, at $x^{eq}_{\beta/L}$, of the horizontal black dashed line (T_{exp}) with the red dashed line (extension of the β liquidus line). When α precipitates, its equilibrium with the melt is described by the α liquidus of the equilibrium phase diagram (green line in Fig. 10), which intersects the T_{exp} line in Fig. 10 at melt composition $x^{eq}_{\alpha/L}$. The composition difference between the two interfaces implies a composition gradient in the in-between liquid film, as schematically illustrated in Fig. 9(b).

Fig. 9(c) illustrates the temperature profile across the liquid film, with the actual temperature constant at T_{exp} shown by the red dashed line and the solidification temperature – as obtained from the α-liquidus and the local composition – shown as the green solid line. It is readily seen that the growing nucleus experiences an increase in supercooling, ΔT, with increasing distance from its interface with the melt. In other words, the growth scenario is one of constitutional supercooling. As a result, planar interfaces may be instable [45] and grow modulations that initiate the formation of a cell structure. Thus, the clusters of ligaments obtained in this work form due to the combined action of both, constitutional supercooling and phase partitioning.

A similar mechanism of constitutional supercooling has been observed in peritectic melting of $Ba_2YCu_3O_{6+\delta}$ during directional heating [30]. However, that study worked with a macroscopic, sample-scale and externally imposed temperature gradient. This is distinct from the present study, where a composition gradient develops spontaneously and internally, at the microscopic scale of the liquid film. In other words, the constitutional supercooling in our scenario results from the composition gradient across the melt, which is maintained by the inverse peritectic reaction. Since the size of this α nucleus and the thickness of the liquid layer are much smaller than the size of initial β grains, the growing α/L region is surrounded by β in every direction. Thus, a radial composition gradient drives the growth of α and results in spheroidal clusters.

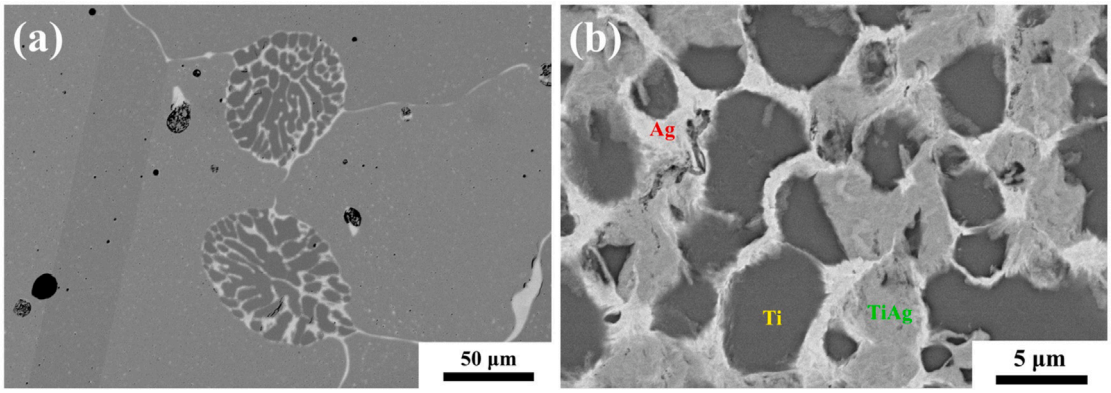

Fig. 11. Comparing microstructures of the reverse peritectic melting of Ni_3Sn_4 and TiAg. Note largely different scale bars. (a) Backscattered electron image of a partially decomposed Ni_3Sn_4 sample, showing spherical clusters of Ni_3Sn_2 ligaments. The original Ni_3Sn_4 grain size is much larger than the Ni_3Sn_2 cell size. (b) Image of a partially decomposed TiAg sample, reproduced from [11]. Three phases can be found including the bright phase as Ag, dark phase as Ti and gray phase as TiAg. The newly formed Ti phase has a similar size as the original TiAg grains.

4.4. Comparing peritectic melting of Ni_3Sn_4 and TiAg

We now return to the differences and commonalities in the microstructure evolution of the two peritectic melting systems, Ni_3Sn_4 and TiAg [11].

Fig. 11 compares the respective morphologies, contrasting the cell structure ensuing from melting of Ni_3Sn_4 with the convex product grains after melting of TiAg. Considering the scale bars in Fig. 11, it is seen that the Ni_3Sn_2 cells and the Ti grains are of quite similar characteristics size. The most obvious distinction between the two systems is then the much larger grain size of the parent phase in Ni_3Sn_4. By contrast, both systems exhibit roughly one crystal of the product phase (cluster or grain) per grain of the parent microstructure. That implies a substantially higher nucleus density in TiAg. This is reasonable, in view of the low interfacial energy, hence low nucleation barrier, of the coherent interfaces in that system.

In Ni_3Sn_4, contrary to the small individual cells, the crystallographically aligned clusters of the product phase grow to much larger size than the randomly oriented grains in TiAg. The large Ni_3Sn_2 clusters require a cellular structure for locally accommodating the liquid product phase. By contrast, the much finer TiAg microstructure affords channeling the liquid product phase into regions in-between the Ti grains, which results in the granular and less ordered appearance of that system's microstructure.

As a commonality of the two peritectic melting reactions, the entry into the two-phase regime takes the form not of a classic, macroscopic melting front that consumes the sample from outside, but rather of internal melting events, distributed uniformly throughout the microstructure. This generates a fine-scale phase mixture, somewhat similar to precipitation from a supersaturated solid solution, but here exhibiting small-scale regions of the liquid phase. Those regions then enable the nucleation and growth of the solid product phase. In the case of NiSn, constitutional supercooling and cellular growth refine the product microstructure. As melting starts at grain boundaries, the grain size determines the initial microstructural length scale in TiAg and NiSn. In principle, scenarios may be envisaged where the nucleation of the melt is governed by the lattice defects, such as dislocation cores. It may then be possible to refine the microstructural length scale that emerges from such distributed internal melting (DIM) processes to values even smaller than that of the present examples.

5. Conclusions

In this work, the intermetallic compound Ni_3Sn_4 is studied as a novel example of liquid film migration during peritectic melting. Spherical clusters of crystallographically aligned Ni_3Sn_2 ligaments are observed, forming a bicontinuous structure with the Sn phase. The microstructure is significantly refined (from around 150 μm to about 2 μm) after phase decomposition. As a remarkable trend, a finer microstructure is obtained by annealing at a higher temperature.

Compared to TiAg, which is the subject of earlier studies, peritectic melting of Ni_3Sn_4 results in a quite different microstructure morphology. We argue that the Ni_3Sn_2 ligaments form through cellular growth driven by constitutional supercooling, which is induced by composition gradient within the liquid layer in the absence of an externally imposed temperature gradient. During the growth of Ni_3Sn_2, a higher driving force (high annealing temperature) leads to shorter diffusion time for atoms within the liquid layer, resulting in a finer microstructure, similar to the case of eutectic growth. These mechanisms, which significantly impact the final microstructure, were largely ignored in previous studies. The findings of this work provide a comprehensive understanding of the peritectic melting process, and offer instructions for simulation studies in this field.

As a particularly noteworthy observation, we re-emphasize that our study confirms peritectic melting as an alternative pathway to micron-scale bicontinuous microstructures. The morphology is quite similar to what results from the widely studied approach of liquid-metal dealloying (LMD), yet peritectic melting brings an enhanced potential for upscaling. This is because the microstructure is formed by local patterning during distributed internal melting (DIM), avoiding the long-range transport during liquid-metal dealloying's corrosive attack from the outside. Bicontinuous microstructures made by partial melting, a process that might be realized in even more alloy systems than peritectic melting, emphasize the potential of DIM as an alternative to LMD.

Declaration of competing interest

The authors declare that they have no known competing financial interests or personal relationships that could have appeared to influence the work reported in this paper.

Acknowledgments

This work was supported by Deutsche Forschungsgemeinschaft, Germany through the Cluster of Excellence EXC 3120/1 BlueMat: Water-Driven Materials - 533771286 and by the China Scholarship Council.

Appendix A. Supplementary data

Supplementary material related to this article can be found online at https://doi.org/10.1016/j.jmrt.2026.02.189.

References

[1] Wada T, Yubuta K, Inoue A, Kato H. Dealloying by metallic melt. Mater Lett 2011;65:1076–8.

[2] Okulov I, Okulov A, Soldatov I, Luthringer B, Willumeit-Römer R, Wada T, Kato H, Weissmüller J, Markmann J. Open porous dealloying-based biomaterials as a novel biomaterial platform. Mater Sci Eng C 2018;88:95–103.

[3] Kim JW, Wada T, Kim SG, Kato H. Enlarging the surface area of an electrolytic capacitor of porous niobium by mgce eutectic liquid dealloying. Scr Mater 2016;122:68–71.

[4] Sohn S, Shi S, Markmann J, Berger SA, Weissmüller J. Compressive behavior and connecting topology of monolithic nanoporous niobium. Mater Res Lett 2024;1–10.

[5] McCue I, Ryan S, Hemker K, Xu X, Li N, Chen M, Erlebacher J. Size effects in the mechanical properties of bulk bicontinuous ta/cu nanocomposites made by liquid metal dealloying. Adv Eng Mater 2016;18:46–50.

[6] Mokhtari M, Wada T, Bourlot C Le, Duchet-Rumeau J, Kato H, Maire E, Mary N. Corrosion resistance of porous ferritic stainless steel produced by liquid metal dealloying of incoloy 800. Corros Sci 2020;166:108468.

[7] Joo S-H, Kato H, Okulov IV. Evolution of 3D interconnected composites of high-entropy TiVNbMoTa alloys and Mg during liquid metal dealloying. Compos Part B 2021;222:109044.

[8] Okulov AV, Joo S-H, Kim HS, Kato H, Okulov IV. Nanoporous high-entropy alloy by liquid metal dealloying. Metals 2020;10:1396.

[9] McCue I, Gaskey B, Geslin P-A, Karma A, Erlebacher J. Kinetics and morphological evolution of liquid metal dealloying. Acta Mater 2016;115:10–23.

[10] Hu W-K, Shao J-C, Wang S-G, Jin H-J. Evolution of a bicontinuous structure in peritectic melting: The simplest form of dealloying. Phys Rev Mater 2019;3:113601.

[11] Li Z, Lührs L, Krekeler T, Weissmüller J. How peritectic melting forms bicontinuous microstructures. Acta Mater 2025;289:120917.

[12] Rabkin E. Liquid film migration in a mo (Ni) bicrystal. Phil Mag Lett 1996;73:187–94.

[13] Young-Joon B, Yoon DN. Migration of liquid film and grain boundary in Mo-Ni induced by temperature change. Acta Metall 1985;33:1911–7.

[14] Barker S, Purdy G. On liquid film migration in aluminium–copper alloys. Acta Mater 1998;46:511–24.

[15] Kuo M, Fournelle R. Diffusion induced grain boundary migration (DIGM) and liquid film migration (LFM) in an Al-2.07 wt% Cu alloy. Acta Metall Mater 1991;39:2835–45.

[16] Kim JK, Yoon DY. The suppression of chemically induced liquid film migration in Co–Cu at high temperature. Acta Metall Mater 1994;42:913–9.

[17] Muschik T, Kaysser W, Hehenkamp T. Melting of Cu–In solid solutions at small superheating by droplet formation and liquid film migration. Acta Metall 1989;37:603–13.

[18] Li Z, Lührs L, Weissmüller J. Bicontinuous microstructure formation through partial melting. Scr Mater 2024;250:116192.

[19] Chaim R, Heuer AH, Brandon DG. Phase equilibration in ZrO2-Y2O3 alloys by liquid-film migration. J Am Ceram Soc 1986;69:243–8.

[20] Schmid HK. Diffusion-induced grain-boundary migration in ceria-stabilized tetragonal zirconia polycrystals. J Am Ceram Soc 1991;74:387–94.

[21] McPhee W, Schaffer G, Drennan J. The effect of iron on liquid film migration and sintering of an Al–Cu–Mg alloy. Acta Mater 2003;51:3701–12.

[22] Ko JY, Park S-Y, Yoon DY, Kang S-JL. Migration of intergranular liquid films and formation of core-shell grains in sintered TiC–Ni bonded to WC–Ni. J Am Ceram Soc 2004;87:2262–7.

[23] Ojo O, Richards N, Chaturvedi M. Liquid film migration of constitutionally liquated γ' in weld heat affected zone (haz) of inconel 738lc superalloy. Scr Mater 2004;51:141–6.

[24] Radhakrishnan B, Thompson R. Liquid film migration (lfm) in the weld heat affected zone (haz) of a ni-base superalloy. Scr Metall Mater 1990;24:537–42.

[25] Peng P. Migration of liquid particle from mushy zone interface in temperature gradient. Int J Heat Mass Transfer 2019;142:118467.

[26] Peng P, Li X, Li J, Su Y, Guo J, Fu H. On migration of primary/peritectic interface during interrupted directional solidification of Sn-Ni peritectic alloy. Sci Rep 2016;6:24512.

[27] Cima MJ, Flemings MC, Figueredo AM, Nakade M, Ishii H, Brody HD, Haggerty JS. Semisolid solidification of high temperature superconducting oxides. J Appl Phys 1992;72:179–90.

[28] Boussinot G, Brener E, Temkin D. Kinetics of isothermal phase transformations above and below the peritectic temperature: Phase-field simulations. Acta Mater 2010;58:1750–60.

[29] Viardin A, Boussinot G, Zollinger J. Phase field modeling of partial remelting during reheating of a multiphase peritectic solidification microstructure. Materialia 2022;26:101590.

[30] Figueredo A, Cima M, Flemings M, Haggerty J. Directional phase formation on melting via peritectic reaction. Metall Mater Trans A 1994;25:1747–60.

[31] Schneider CA, Rasband WS, Eliceiri KW. NIH image to ImageJ: 25 years of image analysis. Nature Methods 2012;9:671–5.

[32] Gražulis S, Daškevič A, Merkys A, Chateigner D, Lutterotti L, Quirós M, Serebryanaya NR, Moeck P, Downs RT, Bail A Le. Crystallography open database (COD): an open-access collection of crystal structures and platform for world-wide collaboration. Nucleic Acids Res 2011;40:D420–7.

[33] Schmetterer C, Flandorfer H, Richter KW, Saeed U, Kauffman M, Roussel P, Ipser H. A new investigation of the system Ni–Sn. Intermetallics 2007;15:869–84.

[34] Fjellvåg H, Kjekshus A, Stomberg R, Zingales R, Vikholm I, Urso F, Weidlein J, Zingaro RA. Structural properties of Co3Sn2, Ni3Sn2 and some ternary derivatives. Acta Chem Scand 1986;40:23–30.

[35] Jeitschko W, Jaberg B. Structure refinement of Ni3Sn4. Struct Sci 1982;38:598–600.

[36] Erlebacher J. An atomistic description of dealloying - porosity evolution, the critical potential, and rate-limiting behavior. J Electrochem Soc 2004;151:C614–26.

[37] Parida S, Kramer D, Volkert CA, Rösner H, Erlebacher J, Weissmüller J. Volume change during the formation of nanoporous gold by dealloying. Phys Rev Lett 2006;97:035504.

[38] Jin HJ, Kurmanaeva L, Schmauch J, Rösner H, Ivanisenko Y, Weissmüller J. Deforming nanoporous metal: Role of lattice coherency. Acta Mater 2009;57:2665–72.

[39] Sieradzki K, Dimitrov N, Movrin D, McCall C, Vasiljevic N, Erlebacher J. The dealloying critical potential. J Electrochem Soc 2002;149:B370–7.

[40] Weissmüller J, Newman RC, Jin HJ, Hodge AM, Kysar JW. Nanoporous metals by alloy corrosion: Formation and mechanical properties. MRS Bull 2009;34:577–86.

[41] Artymowicz DM, Erlebacher J, Newman RC. Relationship between the parting limit for de-alloying and a particular geometric high-density site percolation threshold. Phil Mag 2009;89:1663–93.

[42] Lai L, Gaskey B, Chuang A, Erlebacher J, Karma A. Topological control of liquid-metal-dealloyed structures. Nat Commun 2022;13:2918.

[43] Bieberdorf N, Asta M, Capolungo L. Grain boundary effects in high-temperature liquid-metal dealloying: a multi-phase field study. Npj Comput Mater 2023;9:127.

[44] Geslin PA, McCue I, Gaskey B, Erlebacher J, Karma A. Topology-generating interfacial pattern formation during liquid metal dealloying. Nat Commun 2015;6:8887.

[45] Kurz W, Fisher D, Rappaz M. Fundamentals of solidification. trans tech publications ltd; 2023.